

# The Topographically Bound Low-Level Easterly Jet Surrounding Antarctica

SCOTT R. FULTON \*

*Department of Mathematics, Clarkson University, Potsdam, NY, USA*

WAYNE H. SCHUBERT

*Department of Atmospheric Science, Colorado State University, Fort Collins, Colorado, USA*

ZHENGQING CHEN

*Department of Mathematics, Clarkson University, Potsdam, NY, USA*

PAUL E. CIESIELSKI

*Department of Atmospheric Science, Colorado State University, Fort Collins, Colorado, USA*

## ABSTRACT

This study investigates the topographically bound low-level, easterly jet surrounding Antarctica. This jet is modeled as a balanced flow that obeys the potential vorticity invertibility principle. This invertibility principle is expressed in isentropic coordinates, using local linear balance as the balance condition in the spherical coordinate formulation of the elliptic problem. In this way, the low-level easterly flow around Antarctica can be attributed to the fact that radiative cooling over the Antarctic plateau results in the bending of isentropic surfaces sharply upward at the edge of the plateau and in the production of a shallow potential vorticity anomaly just above the plateau. The dynamical connection of the jet with katabatic winds can be understood through the meridional circulation equation. Model results based on the simple theoretical arguments developed here are found to be consistent with high resolution ECMWF reanalysis data for the 2008–2010 period.

To be submitted to *Journal of the Atmospheric Sciences*

---

## 1. Introduction

---

*Corresponding author address:* Scott R. Fulton, Department of Mathematics, Clarkson University, Potsdam, NY, USA. Email: fulton@clarkson.edu

There are many interesting aspects of the atmospheric flow in the Antarctic region. One is the large baroclinicity and strong westerly flow

that exists between  $35^\circ\text{S}$  and  $60^\circ\text{S}$  throughout the year, with a nearly circular storm track in summer (DJF) and a more asymmetric winter (JJA) storm track that spirals in toward Antarctica, as discussed by Inatsu and Hoskins (2004) and Hoskins and Hodges (2005). A second interesting aspect is the prevalence of Antarctic katabatic winds, which are winds that flow down ice-covered slopes cooled by radiative processes. One of the first maps of the time-averaged surface streamlines for the whole Antarctic continent was produced by Mather and Miller (1967) and later published by Mather (1969). This map, an adapted version of which is presented here as Fig. 1, shows the katabatic flow toward the edge of the continent and its merger with the more geostrophic coastal easterlies, which occur over a nearly flat surface where the katabatic forcing disappears. A simple local theory of this boundary layer flow was developed by Ball (1960). His theory consists of an Ekman-type slab boundary layer of constant depth, topped by a temperature inversion and forced by the overlying pressure gradient force and by the katabatic force, which depends on the local topographic slope. The solutions of the two algebraic slab boundary layer equations show that the resulting katabatic flow is not directly down the slope, but is deflected to the left by the Coriolis force, a feature that is apparent in the observational data shown in Fig. 1. A detailed analysis supporting the validity of this simple model was provided by Parish and Bromwich (1987), who computed local model solutions on a  $50\text{ km} \times 50\text{ km}$  grid over the entire continent, using refined topographic data for computation of the local topographic slopes. The model results generally agree with the observations shown in Fig. 1, but with additional detail, especially in coastal valleys. For further discussion of these topics and of Antarctic meteorology and climatology in general, the reader is referred to the comprehensive review given in the monograph by King and Turner (1997).

The Antarctic flow feature of primary attention here is the circumpolar, low-level easterly circula-

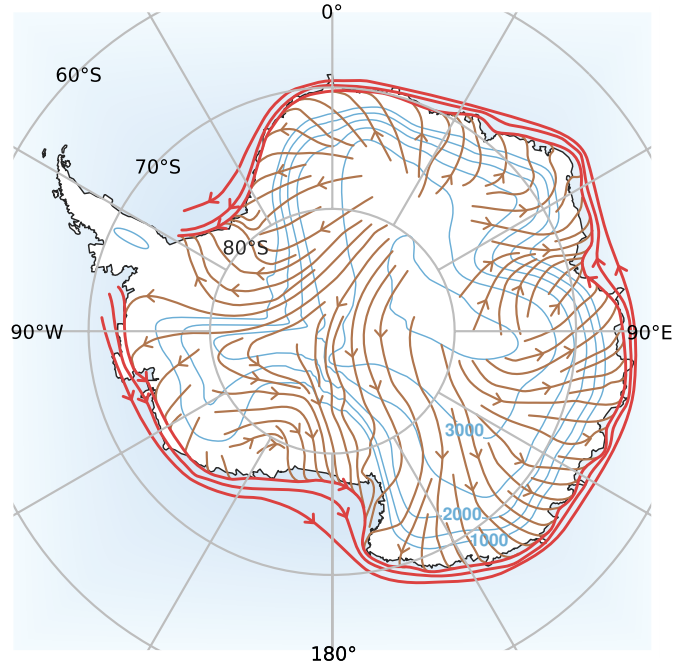


FIG. 1. Topographic contours, labeled in meters, are shown by the blue lines. Time-averaged streamlines of the surface wind over the continent are shown by the brown lines. Streamlines of the coastal easterlies are shown in red. Note that the time-averaged surface flow is not directly down the local slope, but is deflected to the left by the Coriolis force. Adapted from Fig. 2.4 of Mather and Miller (1967).

tion around the Antarctic periphery, which is indicated by the red streamlines in Fig. 1. The vertical structure of this easterly flow is clearly evident in the reanalysis datasets produced by operational centers. Recently, an improved, high-resolution dataset for the Antarctic region has been provided by the European Centre for Medium-Range Weather Forecasts (ECMWF) from the ‘Year of Tropical Convection (YOTC) reanalysis project (May 2008 to April 2010), as described by Waliser et al. (2012). The part of this dataset used here has 6 h time resolution and  $1.0^\circ \times 1.0^\circ$  horizontal resolution, with 15 irregularly spaced vertical levels between 1000 and 100 hPa. Figure 2 shows the mean winds and mean geopotential at 600 hPa in

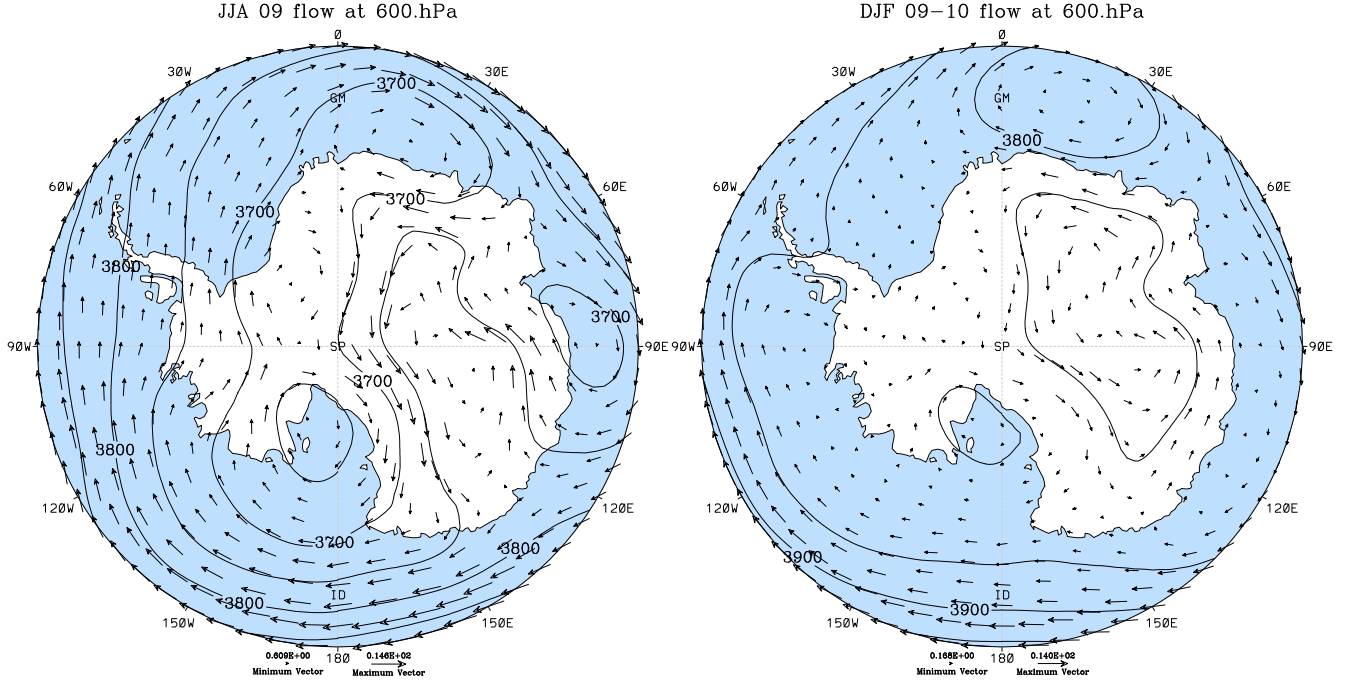


FIG. 2. Mean wind and geopotential fields at 600 hPa from the YOTC analysis for the 2009 cold season (JJA, left panel) and 2009–2010 warm season (DJF, right panel). The outer edge of each map is at 60° S, with the Greenwich meridian at the top. The maximum wind speeds, indicated by the reference vectors at the bottom, are  $14.6 \text{ m s}^{-1}$  (JJA) and  $14.0 \text{ m s}^{-1}$  (DJF). The black contours are for geopotential with 50 m contour intervals.

the Antarctic region, for the austral cold season 1 June 2009 to 31 August 2009 (denoted by JJA, left panel) and austral warm season 1 December 2009 to 28 February 2010 (denoted by DJF, right panel). In addition to the strong westerly flow near 60° S (which is the outer edge of each map), a striking feature of both seasons is the anticyclonic flow that occurs over the elevated terrain of east Antarctica. Associated with this anticyclone is an easterly flow along the eastern edge of the continent. While the cyclone over the Ross Ice Shelf (80° S, 165° W) is considerably stronger during the cold season, the structure and strength of the anticyclone over east Antarctica is similar in the two seasons.

Figure 3 shows latitude-pressure cross sections averaged over the longitude sector 80–100° E for JJA (left panels) and DJF (right panels), with mean isentropes shown by the solid contours. This

particular longitude band was chosen because of its zonal symmetry. Given the vertical resolution of the analysis, fifteen levels are used in ocean regions and approximately eight levels are used in regions of high topography. The top panels show zonal winds in color. At this longitude the topographically bound easterly flow at the edge of the continent is clearly seen, with a peak easterly zonal velocity of  $14.2 \text{ m s}^{-1}$  in the cold season (JJA) and  $11.3 \text{ m s}^{-1}$  in the warm season (DJF). It should be noted that these cross sections are means over three months and twenty degrees of longitude; for individual days and longitudes this easterly low-level jet (LLJ) can be considerably stronger. The bottom panels show corresponding cross sections of potential vorticity (PV). Of particular interest is the region of sharply enhanced PV immediately atop the polar plateau. This region, present in both seasons, is considerably

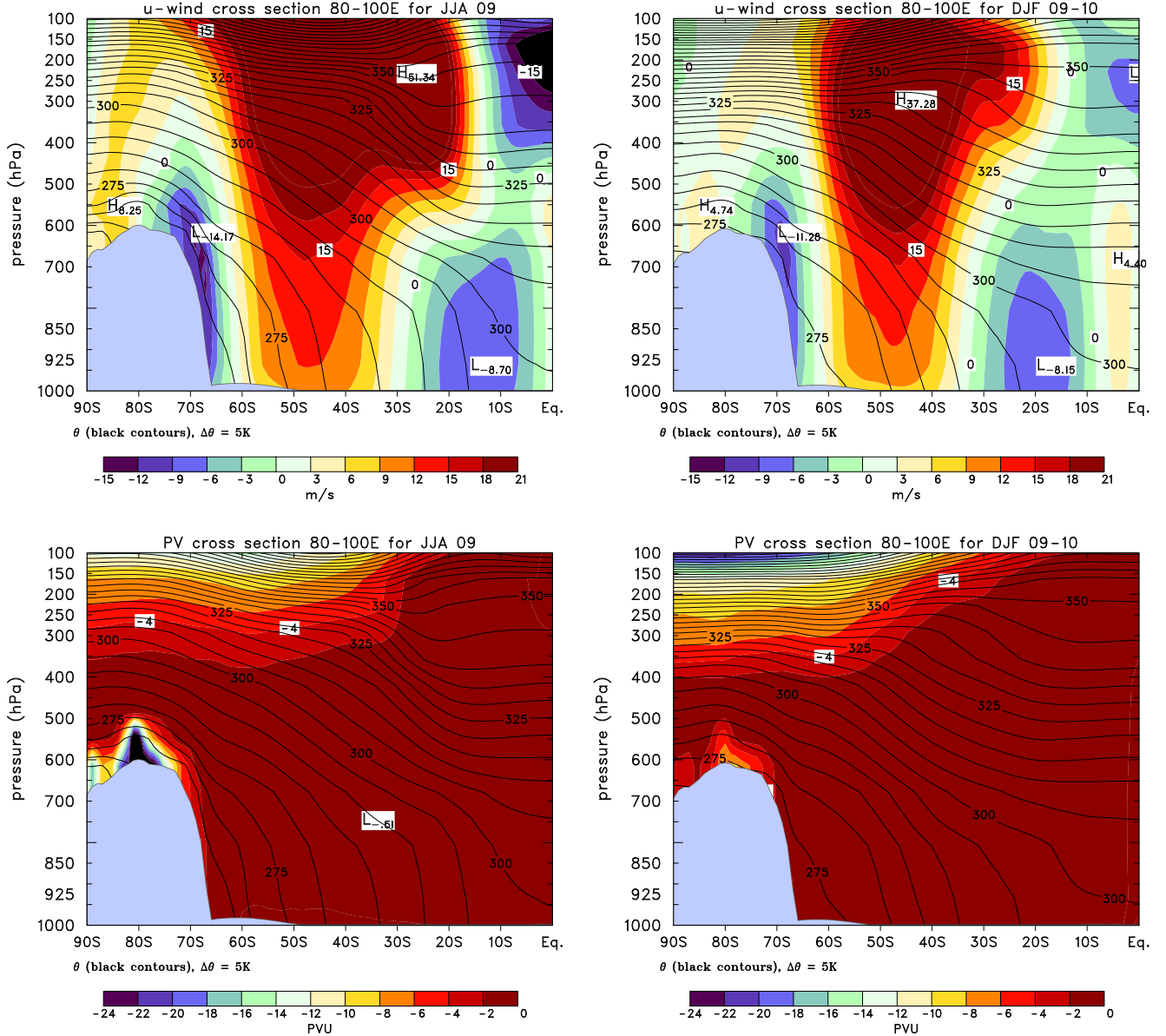


FIG. 3. Mean latitude-pressure cross sections averaged over the longitude sector 80–100° E from the YOTC analysis for the cold season (JJA, left panels) and warm season (DJF, right panels). The top panels show zonal wind with magnitude given by the colorbar, which (for clarity) ends at 21  $\text{m s}^{-1}$ , even though the upper level westerlies are stronger. The bottom panels show PV with magnitude given by the colorbar, where one PV unit is defined as  $10^{-6} \text{ m}^2 \text{ s}^{-1} \text{ K kg}^{-1}$ . Black contours in each panel are isentropes at 5 K intervals.

stronger in the cold (JJA) season, and may be attributed to the strong radiative cooling during the polar night.

In the present paper we shall interpret these

zonal flow patterns in terms of a zonally symmetric, potential vorticity invertibility principle. In this interpretation, three important specified functions are the topography, the potential tempera-

ture along the topography, and the PV in the interior of the domain. Note in Fig. 3 that the 265 K isentrope nearly follows the Antarctic topography in the cold season (JJA), while the 275 K isentrope nearly follows the topography in the warm season (DJF). Thus, to a first approximation, we can regard Antarctica as an isentropic obstacle during the entire year. However, away from the continent, the lower boundary is not isentropic, with the surface value of potential temperature increasing by 25 to 35 K from the edge of the continent to the equator. Note that the larger increase during the cold season is associated with a stronger mid-latitude westerly jet through thermal wind balance and with the large increase in the surrounding sea-ice during austral winter.

The theoretical basis of the present work was given by Eliassen (1980), who studied the topographically bound, balanced response of a rotating, stratified fluid to orography, and by Silvers and Schubert (2013), who applied these ideas to the low-level flows surrounding the Andes. The purpose of the present paper is to extend the analysis of Silvers and Schubert (2013) to the Antarctic region, and thereby to demonstrate that the Antarctic low-level easterly jet can be interpreted as a balanced flow attributed, through the potential vorticity invertibility principle, primarily to the distribution of topography, to the fact that potential temperature varies little along this topography, and to the PV anomaly that resides just above the elevated ice sheet. The outline of the paper is as follows. Section 2 presents the invertibility principle in isentropic coordinates. Section 3 describes a “null case” which serves both as a test of the solution procedure and as a conceptual initial state. The balanced flow induced by an isentropic polar plateau is investigated in section 4, and the effects of surface potential temperature and top pressure variations are investigated in section 5. Section 6 considers the dynamical connections between radiative cooling, katabatic winds, and the easterly jet. Concluding remarks are given in section 7.

## 2. Invertibility principle

Following the arguments of Smith (1979), a simple model of the Antarctic easterly flow was developed by Kottmeier and Stuckenberg (1986), who used an  $f$ -plane argument based on the invertibility of quasi-geostrophic potential vorticity under the assumption that there are no potential vorticity anomalies in the interior of the fluid but that the lowermost isentropic surface has been bowed upward by the topography (an approximate quasi-geostrophic lower boundary condition). Although the model of Kottmeier and Stuckenberg has many approximations, it produces results that agree fairly well with observations that were available at that time, such as those found in Zwally et al. (1983). The PV analysis given here is in the same spirit as the quasi-geostrophic analysis given by Kottmeier and Stuckenberg, but the present analysis bypasses many of the approximations used in quasi-geostrophic theory. In particular, the analysis given here involves a more accurate form of the PV and a more accurate treatment of the lower boundary condition.

The analysis begins by considering hydrostatic motions of a compressible stratified fluid on the sphere. Using the longitude  $\lambda$  and the latitude  $\phi$  as the horizontal coordinates, and the potential temperature  $\theta$  as the vertical coordinate, the potential vorticity  $P(\lambda, \phi, \theta)$  is given by

$$P = \frac{g(f + \zeta)}{\sigma}, \quad (1)$$

where  $f = 2\Omega \sin \phi$  is the Coriolis parameter,  $\sigma(\lambda, \phi, \theta) = -\partial p / \partial \theta$  the pseudo-density,  $p(\lambda, \phi, \theta)$  the pressure,  $g$  the acceleration of gravity, and where

$$\zeta = \frac{\partial v}{a \cos \phi \partial \lambda} - \frac{\partial(u \cos \phi)}{a \cos \phi \partial \phi} \quad (2)$$

is the isentropic relative vorticity, computed from the zonal flow component  $u(\lambda, \phi, \theta)$  and the meridional flow component  $v(\lambda, \phi, \theta)$ , with  $a$  and  $\Omega$  the radius and rotation rate of the earth. Using the ideal gas law to express the density as  $\rho = p / (RT) = c_p p / (R\theta\Pi)$ , where  $\Pi = c_p(p/p_0)^{R/c_p}$

(with  $p_0$  denoting the constant reference pressure,  $R$  the gas constant, and  $c_p$  the specific heat at constant pressure), it is easily shown that  $\theta\rho(d\Pi/dp) = 1$ . This allows (1) to be written in the form

$$\frac{g}{\theta\rho P}(f + \zeta) + \frac{\partial\Pi}{\partial\theta} = 0. \quad (3)$$

The components of the nondivergent part of the flow, denoted by  $u_\psi$  and  $v_\psi$ , are related to the streamfunction  $\psi(\lambda, \phi, \theta)$  by

$$(u_\psi, v_\psi) = \left( -\frac{\partial\psi}{a\partial\phi}, \frac{\partial\psi}{a\cos\phi\partial\lambda} \right), \quad (4)$$

so that the isentropic relative vorticity can be expressed as

$$\begin{aligned} \zeta &= \frac{\partial v_\psi}{a\cos\phi\partial\lambda} - \frac{\partial(u_\psi\cos\phi)}{a\cos\phi\partial\phi} \\ &= \frac{\partial^2\psi}{a^2\cos^2\phi\partial\lambda^2} + \frac{\partial}{a\cos\phi\partial\phi} \left( \cos\phi\frac{\partial\psi}{a\partial\phi} \right) \\ &= \nabla^2\psi. \end{aligned} \quad (5)$$

Using this result and the hydrostatic relation  $\Pi = \partial M/\partial\theta$ , where  $M = \theta\Pi + \Phi$  is the Montgomery potential and  $\Phi$  is the geopotential, we can rewrite (3) as

$$\frac{g}{\theta\rho P}(f + \nabla^2\psi) + \frac{\partial^2 M}{\partial\theta^2} = 0. \quad (6)$$

When isentropic surfaces intersect the earth's surface, they can be considered to run along the earth's surface with a pressure equal to the surface pressure, thereby forming a massless layer with infinite potential vorticity (i.e.,  $\sigma \rightarrow 0$  and  $P \rightarrow \infty$ ). We define  $\theta_S(\lambda, \phi)$  as the actual value of potential temperature on the earth's surface, and work on a domain in  $\theta$  bounded by constants  $\theta_B$  and  $\theta_T$  satisfying  $\theta_B \leq \theta_S(\lambda, \phi) < \theta_T$  over the horizontal domain of interest. Then the region  $\theta_B \leq \theta < \theta_S(\lambda, \phi)$  is the massless layer and the region  $\theta_S(\lambda, \phi) < \theta \leq \theta_T$  is the atmosphere. We use the subscript  $S$  to denote surface values (i.e., values at  $\theta = \theta_S$ ) of other fields. Then in the massless layer,  $\sigma = 0$ ,  $p = p_S$ ,  $\Pi = \Pi_S$ ,  $\Phi = \Phi_S$ , and  $M = \theta\Pi_S + \Phi_S$ . All mass variables other than  $\sigma$

are continuous at  $\theta_S$ . The usual relations between the mass variables hold in the massless layer; a careful analysis (Fulton and Schubert 1991, appendix) shows that the hydrostatic equation also holds at  $\theta = \theta_S$ . While (6) holds in the atmosphere ( $\theta > \theta_S$ ), it reduces to

$$\frac{\partial^2 M}{\partial\theta^2} = 0 \quad (7)$$

in the massless layer ( $\theta < \theta_S$ ) since  $P \rightarrow \infty$  there.

Equations (6) and (7) relate the potential vorticity field  $P(\lambda, \phi, \theta)$ , the wind field  $\psi(\lambda, \phi, \theta)$ , and the mass field  $M(\lambda, \phi, \theta)$ . To convert these into an invertibility relation we now introduce a balance condition between  $\psi$  and  $M$ . The relation between the wind field and the mass field is assumed to be local linear balance, which is discussed in several different contexts by Kuo (1959), Charney and Stern (1962), and Schubert et al. (2009). The isentropic coordinate version of local linear balance is

$$M(\lambda, \phi, \theta) = \tilde{M}(\theta) + f\psi(\lambda, \phi, \theta), \quad (8)$$

where  $\tilde{M}(\theta)$  is a specified reference state, corresponding to pressure  $\tilde{p}(\theta)$ , density  $\tilde{\rho}(\theta)$ , and pseudo-density  $\tilde{\sigma}(\theta) = -d\tilde{p}/d\theta$ , satisfying

$$\frac{d\tilde{M}}{d\theta} = \tilde{\Pi} = c_p \left( \frac{\tilde{p}}{p_0} \right)^{R/c_p}, \quad \tilde{\rho} = \frac{p_0}{R\theta} \left( \frac{\tilde{\Pi}}{c_p} \right)^{c_v/R}, \quad (9)$$

with  $\tilde{M}(\theta_B) = c_p\theta_B$ , and with  $c_v = c_p - R$  denoting the specific heat at constant volume. Using the balance condition (8) in (6) and (7), we can write the invertibility relation in the form

$$\alpha\nabla^2\psi + f\frac{\partial^2\psi}{\partial\theta^2} = \frac{\tilde{\sigma}}{\theta\tilde{\rho}} - \alpha f, \quad (10)$$

where

$$\alpha = \begin{cases} \frac{g}{\theta\rho P}, & \theta_S < \theta < \theta_T \quad [\text{atmosphere}], \\ 0, & \theta_B < \theta < \theta_S \quad [\text{massless layer}]. \end{cases} \quad (11)$$

Since  $\alpha$  depends on  $\rho$  through (11) and since  $\rho$  depends on  $\psi$  through

$$\rho = \frac{p_0}{R\theta} \left( \frac{\Pi}{c_p} \right)^{c_v/R}, \quad \Pi = \tilde{\Pi} + f\frac{\partial\psi}{\partial\theta}, \quad (12)$$

equation (10) is quasi-linear. It is elliptic if  $\alpha$  and  $f$  have the same sign, i.e., if  $P < 0$  in the southern hemisphere and  $P > 0$  in the northern hemisphere. A discussion of the shallow water version of (10) has been given by Schubert et al. (2009), who show how spheroidal harmonic basis functions can be used to obtain analytical solutions, and who also show that the Rossby-Haurwitz wave dispersion curves derived using (10) closely agree with those obtained from the primitive equations. In addition, a discussion of the equatorial  $\beta$ -plane version of (10) has been given by Schubert and Masarik (2006), who illustrate its usefulness in understanding the equatorial Rossby gyres on the west side of the convective envelope in the Madden-Julian Oscillation (MJO). Thus, experience has shown that we can regard (10) as an invertibility principle that is valid over the entire sphere.

We wish to solve the invertibility relation on the region  $\phi_S < \phi < \phi_N$ , where  $\phi_S = -\pi/2$  is the south pole and  $\phi_N$  is a fixed latitude. For the lateral boundary condition we specify  $M$  as in the reference state (17) below, except with  $\theta_B$  replaced by  $\theta_S(\phi_N)$ , and compute Dirichlet values of  $\psi$  accordingly. For the upper boundary condition we specify the pressure  $p_T(\lambda, \phi) = p(\lambda, \phi, \theta_T)$  on the upper isentropic surface  $\theta = \theta_T$ , leading to

$$f \left( \frac{\partial \psi}{\partial \theta} \right) = \Pi_T - \tilde{\Pi}_T \quad \text{at } \theta = \theta_T, \quad (13)$$

where  $\Pi_T(\lambda, \phi)$  corresponds to the specified top pressure. For the lower boundary condition we apply the general relation  $M - \theta(\partial M / \partial \theta) = \Phi$  at  $\theta = \theta_B$ , resulting in

$$f \left( \psi - \theta \frac{\partial \psi}{\partial \theta} \right) = \Phi_S \quad \text{at } \theta = \theta_B, \quad (14)$$

where the surface geopotential  $\Phi_S(\lambda, \phi)$  is specified, giving the topography.

In summary, the invertibility problem consists of (10)–(14). To solve the problem for  $\psi(\lambda, \phi, \theta)$ , we must specify the constants  $\theta_B$ ,  $\theta_T$ ,  $\phi_N$ , the reference state, the potential vorticity  $P(\lambda, \phi, \theta)$

on the domain, and the boundary data  $\theta_S(\lambda, \phi)$ ,  $\Phi_S(\lambda, \phi)$ , and  $p_T(\lambda, \phi)$ .

For simplicity we now restrict our attention to the two-dimensional version of (10)–(14) under the assumption that all fields are independent of longitude.<sup>1</sup> In this case the Laplacian (5) reduces to

$$\nabla^2 \psi = \frac{1}{\cos \phi} \frac{\partial}{\partial \phi} \left( \cos \phi \frac{\partial \psi}{\partial \phi} \right). \quad (15)$$

This operator is singular at the poles  $\phi = \pm\pi/2$ ; since by symmetry  $\partial\psi/\partial\phi = 0$  there, we can use L'Hôpital's Rule to replace (15) by the limiting form

$$\nabla^2 \psi = \frac{2}{a^2} \frac{\partial^2 \psi}{\partial \phi^2} \quad \text{at } \phi = \pm \frac{\pi}{2}. \quad (16)$$

The numerical method used to solve this problem is described in the Appendix.

For the results presented below we will take the northern boundary to be  $\phi_N = -20^\circ$ , and unless otherwise noted we will take the top pressure  $p_T$  to be constant. The reference state is taken to be

$$\tilde{M}(\theta) = \Pi_B \theta - \frac{(\Pi_B - \Pi_T)}{2(\theta_T - \theta_B)} (\theta - \theta_B)^2, \quad (17)$$

which gives  $\Pi$  linear in  $\theta$  and buoyancy frequency inversely proportional to  $\theta$  as in Silvers and Schubert (2013). The constants are given by  $\theta_B = 260$  K and  $\theta_T = 370$  K, with  $\Pi_B$  and  $\Pi_T$  based on  $p_B = p_0 = 1000$  hPa and  $p_T = 100$  hPa.

### 3. Null case

A useful test of the solution procedure is as follows. If we specify  $P = \tilde{P} = gf/\tilde{\sigma}$ , then  $\psi = 0$  solves (10) in the atmosphere. If  $\psi = 0$  also satisfies the boundary conditions, then there is no flow. This occurs when  $\theta_S$  and  $\Phi_S$  are specified such that

$$\tilde{\Phi}(\theta_S(\phi)) = \Phi_S(\phi). \quad (18)$$

Then  $\psi = 0$  solves (10) in the atmosphere and satisfies the lower boundary condition at  $\theta = \theta_S$ ,

<sup>1</sup>An insightful discussion of the usefulness of the zonal-symmetry approximation has been given by Egger (1985).

so there is no flow in the atmosphere. With the reference state (17), (18) reduces to

$$\theta_S(\phi) = \left[ \theta_B^2 + \frac{(\Pi_B - \Pi_T)}{2(\theta_T - \theta_B)} \Phi_S(\phi) \right]^{1/2}. \quad (19)$$

Figure 4 shows the solution of this “null case”, where the surface topography is given in the next section by equation (20). As expected, the mass field is horizontally homogeneous and the zonal wind is essentially zero outside the massless region. The anticyclone in the massless region of Fig. 4 (bottom panel) has no physical significance and, in fact, is squashed into oblivion in the  $(\phi, p)$ -space depiction shown in the top panel. However, it is important to keep in mind that, in order to produce Fig. 4, the PV invertibility problem has been solved in  $(\phi, \theta)$ -space in the domain  $-90^\circ \leq \phi \leq -20^\circ$ ,  $260 \text{ K} \leq \theta \leq 370 \text{ K}$ , i.e., in the entire domain shown in the bottom panel. Thus, the computational domain includes points that lie in the massless region at the lower left of the bottom panel. The calculations performed in this massless region can be considered the overhead cost for the convenience of working in a computational domain that has the isentropic surface  $\theta = 260 \text{ K}$  as the lower boundary. It is also important to note that, while there is infinite PV in the massless region, it does not induce any zonal flow in atmosphere (i.e., outside the massless region) because the specified functions  $\Phi_S(\phi)$ ,  $\theta_S(\phi)$ , and  $\tilde{\Phi}_S(\theta)$  satisfy (18).

The null case shown in Fig. 4 is obviously quite different than the observations shown in Fig. 3. However, we may consider Fig. 4 to be a conceptual “initial state” as follows. Starting with the situation of the null case, consider how the atmosphere would respond to radiative cooling of the polar plateau. With  $\dot{\theta} < 0$  on the top and slope of the plateau, isentropes would be forced locally upward. If the cooling were slow, a balanced secondary (meridional) circulation would develop. If the cooling were fast, the response would be more complicated and involve propagating gravity-inertia waves superimposed on the bal-

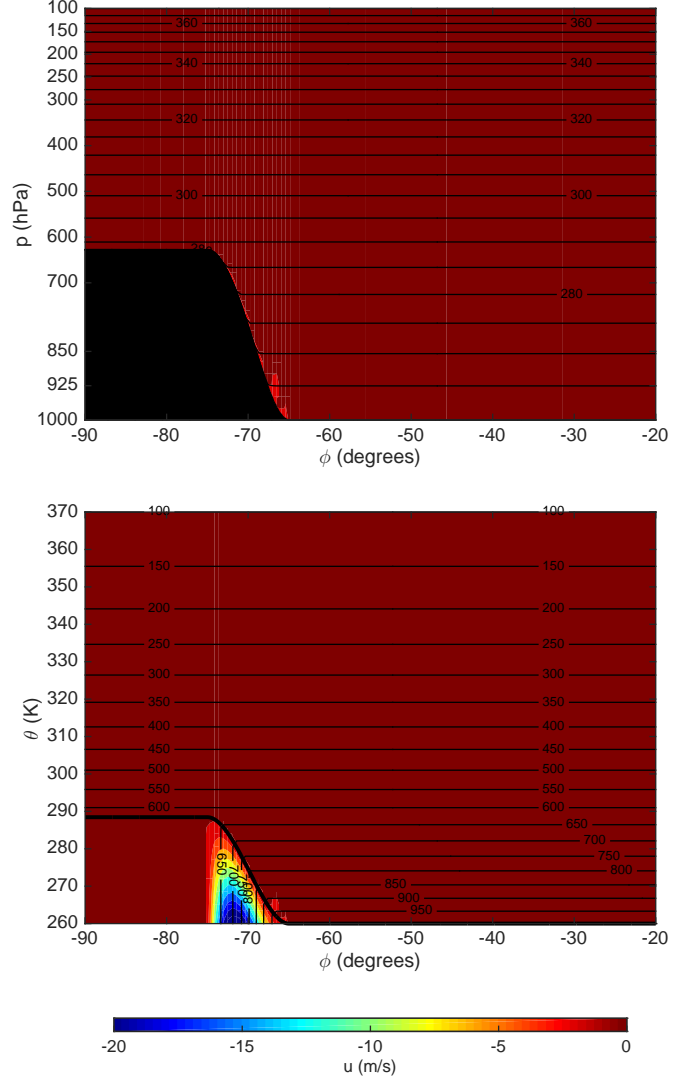


FIG. 4. Zonal wind field (shading,  $2 \text{ m s}^{-1}$  intervals) for the null case described in the text. The massless layer is indicated in  $(\phi, p)$  space (top panel) by the black region along the lower boundary, and in  $(\phi, \theta)$  space (bottom panel) by the thick black line corresponding to  $\theta_S(\phi)$ . Black lines are isentropes (top panel, spacing 5 K) and isobars (bottom panel, spacing 50 hPa).

anced secondary circulation. Thus, for simplicity, suppose the cooling is slow.

Since the concentrated radiative cooling at the mountain surface moves mass downward across isentropic surfaces, in the  $(\phi, p)$ -space view of

Fig. 4 the  $\theta$  surfaces creep upward along the mountain slope and the  $\theta = 285$  K surface, which initially was at the mountain crest, is pushed upward into the free atmosphere above the crest. In the  $(\phi, \theta)$ -space view of Fig. 4, the top of the massless layer shifts downward from  $\theta = 285$  K to  $\theta = 284$  K, say. In other words, the radiative cooling is acting to remove the massless layer. Because the slowly changing meridional circulation is governed by an elliptic partial differential equation, the effects of the concentrated radiative cooling will spread both horizontally (over a Rossby length) and vertically (over a Rossby depth). The equatorward meridional flow on and near the mountain slope (i.e., the katabatic wind) will be deflected to the left by the Coriolis effect, thereby producing a low-level easterly jet around the periphery of the continent. After a sufficient time, isentropes will have crept upward until a nearly isentropic barrier exists, i.e., the massless layer has almost completely disappeared. Note that the PV invertibility view of this scenario is very succinct. It simply finds the strength and spatial structure of the easterly jet given the mountain profile, the distribution of  $\theta$  along the earth’s surface, the PV distribution in the interior, and the boundary conditions at the top and lateral boundaries.

#### 4. Isentropic polar plateau

In this section we consider the case in which there is a polar plateau, but the lower boundary is an isentropic surface, i.e.,  $\theta_S(\phi) = \theta_B$ , so there is no massless layer. The geopotential at the lower boundary varies from  $gH$  at  $\phi_a$  to 0 at  $\phi_b$  via

$$\Phi_S(\phi) = gH \begin{cases} 1, & \phi_S \leq \phi \leq \phi_a, \\ S_\Phi \left( \frac{\phi - \phi_a}{\phi_b - \phi_a} \right), & \phi_a \leq \phi \leq \phi_b, \\ 0, & \phi_b \leq \phi \leq \phi_N, \end{cases} \quad (20)$$

where  $S_\Phi(s) = 1 - 3s^2 + 2s^3 = S_\theta(1 - s)$  is a cubic Hermite function giving a smooth transition from 1 at  $s = 0$  to 0 at  $s = 1$ . This specification of

$\Phi_S(\phi)$  is designed to give a rough approximation to the actual topography of Antarctica at longitude  $90^\circ$  E. For the calculations presented here we use  $H = 3500$  m,  $\phi_a = -75^\circ$ , and  $\phi_b = -65^\circ$  unless otherwise noted.

For the potential vorticity, we first define a “background” potential vorticity  $\bar{P}(\phi, \theta) = gf(\phi)/\bar{\sigma}(\phi, \theta)$  with  $\bar{\sigma}$  computed as for the reference state (17), except with  $\theta_B$  replaced by  $\theta_S(\phi)$  and  $\Pi_T$  computed from  $p_T(\phi)$ .<sup>2</sup> With this PV distribution the solution of the invertibility problem (not shown) exhibits an easterly jet along the slope of the plateau as expected; however, the wind speeds are unrealistically high, as are the pressures in the area of the plateau. This is remedied by including a region of enhanced PV on top of the plateau as present in the YOTC analysis shown in Fig. 3 to account for the strong radiative cooling over the polar plateau. Using Fig. 3 (JJA of 2009) as a guide, this is specified as a Gaussian function with amplitude  $-18.6$  PV units and  $e$ -folding width  $10^\circ$  in latitude and  $20$  K in  $\theta$ , centered at  $\phi = -85^\circ$  and  $\theta = \theta_B$ . This specification of PV is used for all subsequent results.

Figure 5 shows the zonal wind field that results from this isentropic polar plateau. The low-level easterly jet is clearly captured in this solution, with input based only on the topography of the plateau and the region of enhanced PV above it. The jet is stronger than in the YOTC analysis of Fig. 3, but that is due in part to the lack of surface friction in the model. The weaker westerly flow on the top of the plateau is in qualitative agreement with the data.

In Fig. 5 the lower boundary is isentropic: the isentropes along the plateau and slope parallel the surface. However, shown by Eliassen (1980) and further explored by Silvers and Schubert (2013), with higher or steeper terrain it is possible for the topography to puncture the lower isentropes. This occurs in the case studied here, even with  $\theta_S(\phi) = \theta_B$  specified. Figure 6 shows the flow

<sup>2</sup>This definition anticipates cases with variable  $\theta_S(\phi)$  and  $p_T(\phi)$  below; for the isentropic case here,  $\bar{P} = \tilde{P}$ .

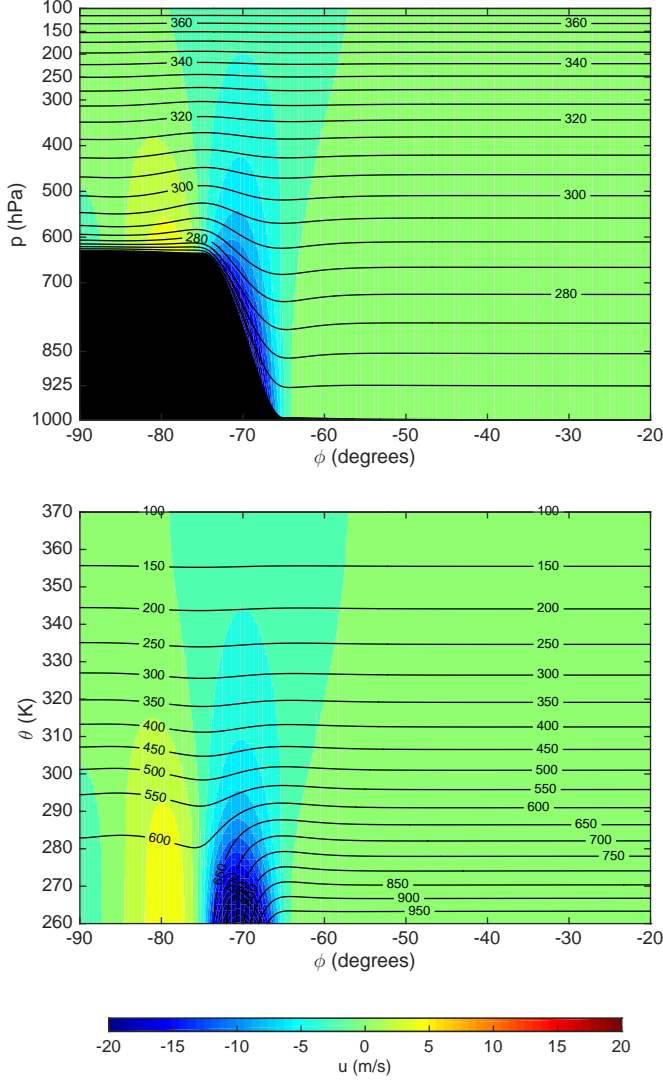


FIG. 5. Zonal wind field (shading,  $2 \text{ m s}^{-1}$  intervals) for the case of an isentropic polar plateau. Isentropes in  $(\phi, p)$  space (top panel) and isobars in  $(\phi, \theta)$  space (bottom panel) are as in Fig. 4. The maximum easterly wind is  $28.3 \text{ m s}^{-1}$ , with a maximum westerly wind of  $5.3 \text{ m s}^{-1}$  above the plateau.

obtained for a steeper plateau (top panel) and a higher plateau (bottom panel). In both cases the easterly jet is considerably stronger and the lower isentropes intersect the surface near the top edge of the plateau, indicating that the critical steepness or height, respectively, has been exceeded.

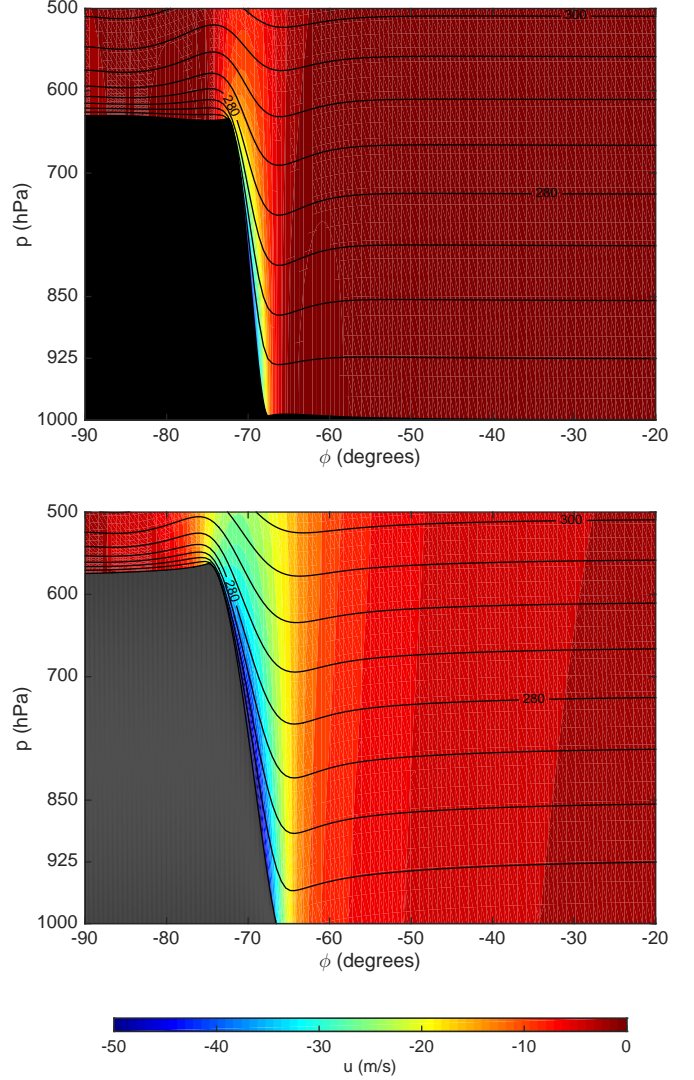


FIG. 6. Zonal wind field (shading,  $2 \text{ m s}^{-1}$  intervals) for isentropic polar plateaus as in Fig. 5 but steeper (top panel, where  $\phi_a = -72.5^\circ$  and  $\phi_b = -67.5^\circ$ ) or higher (bottom panel, where  $H = 5000 \text{ m}$ ). The maximum easterly winds are  $48.6 \text{ m s}^{-1}$  and  $58.1 \text{ m s}^{-1}$ , respectively. Only the lower portion of the domain is shown for clarity.

## 5. Effects of other forcing

The results above show that the easterly LLJ surrounding Antarctica can be explained as the balanced flow induced by an isentropic polar plateau with a PV anomaly due to radiative cooling. In this section we investigate the effects of

two other forcing terms for this problem, namely, the variations of surface potential temperature  $\theta_S$  and the top pressure  $p_T$ .

First, consider the case in which the potential temperature on the lower boundary varies from  $\theta_B$  at  $\phi_c$  to  $\theta_B + \Theta$  at  $\phi_d$  via

$$\theta_S(\phi) = \theta_B + \Theta \begin{cases} 0, & \phi_S \leq \phi \leq \phi_c, \\ S_\theta \left( \frac{\phi - \phi_c}{\phi_d - \phi_c} \right), & \phi_c \leq \phi \leq \phi_d, \\ 1, & \phi_d \leq \phi \leq \phi_N, \end{cases} \quad (21)$$

where  $S_\theta(s) = 3s^2 - 2s^3$  is a cubic Hermite function giving a smooth transition from 0 at  $s = 0$  to 1 at  $s = 1$ . This specification of  $\theta_S(\phi)$  is designed to roughly fit the YOTC analysis for the cold season (JJA) shown in Fig. 3, with a smooth extrapolation into the south polar region that is actually covered by elevated terrain. For the calculations presented here the values  $\phi_c = -70^\circ$ ,  $\phi_d = -20^\circ$ , and  $\Theta = 35$  K are used.

Figure 7 shows the balanced flow obtained for this case, both without topography (top panel) and with (bottom panel) the polar plateau of section 4 (and the associated enhanced PV). It is apparent that the variation in surface potential temperature accounts for the upper-level westerly flow in the analysis of Fig. 3, but has little effect on the easterly LLJ. In this case there is a significant massless layer in the computational domain in  $(\phi, \theta)$  space, but the westerly flow within it (not shown) is fictitious, as in the null case of section 3.

Up to this point all results have been computed using an isobaric top. However, the YOTC analysis shown in Fig. 3 has considerable variation of pressure along the  $\theta_T = 370$  K surface. Figure 8 shows the balanced flow for the same cases as in Fig. 7 but with top pressure smoothly varying (using cubic Hermite functions) from  $p_T = 100$  hPa at  $\phi = -80^\circ$  to 155 hPa at  $\phi = -50^\circ$ , and back to 100 hPa at  $\phi = -20^\circ$ ; this variation approximates that of the cold season (JJA) analysis in Fig. 3. The solution is qualitatively similar, but the variation in top pressure has weakened the upper-level westerly jet from  $38.0$  to  $31.0$   $\text{m s}^{-1}$ .

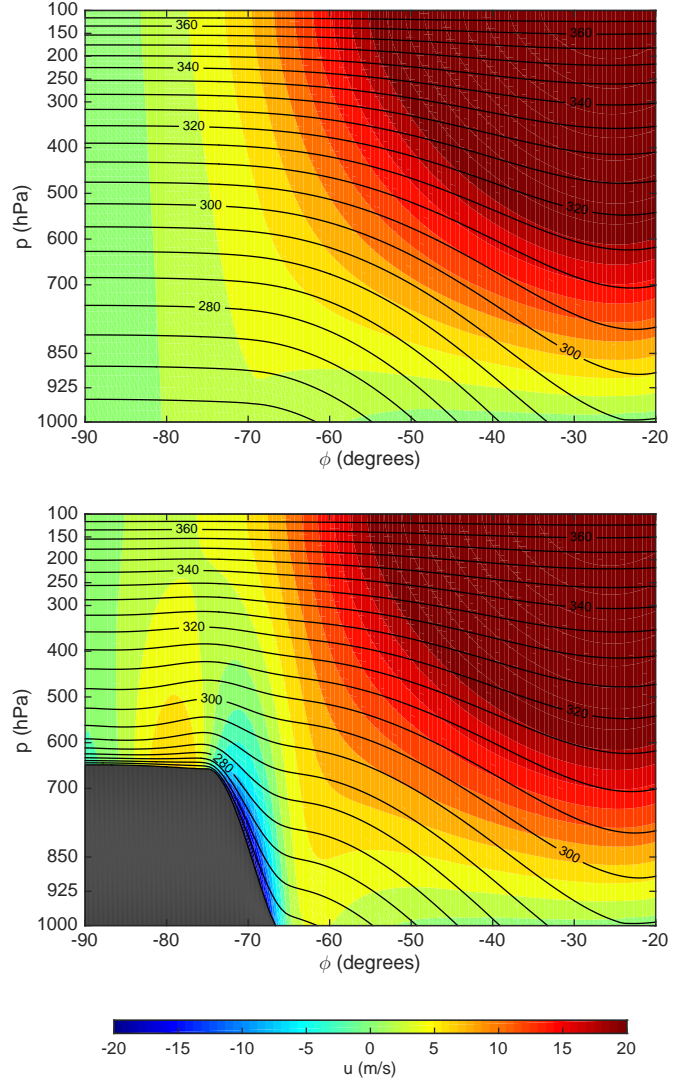


FIG. 7. Zonal wind field (shading,  $2 \text{ m s}^{-1}$  intervals) for with surface potential temperature increasing by  $\Theta = 35$  K from  $\phi_c = -70^\circ$  to  $\phi_d = -20^\circ$ , both without topography (top panel) and with a polar plateau (bottom panel). Black lines are isentropes with spacing 5 K. The maximum westerly wind is approximately  $38 \text{ m s}^{-1}$ ; in the LLJ (bottom panel) the maximum easterly wind is  $24.4 \text{ m s}^{-1}$ .

## 6. Dynamical connections between radiative cooling, katabatic winds, and the easterly jet

The PV invertibility principle given in (10)–(14) provides a mathematical foundation for un-

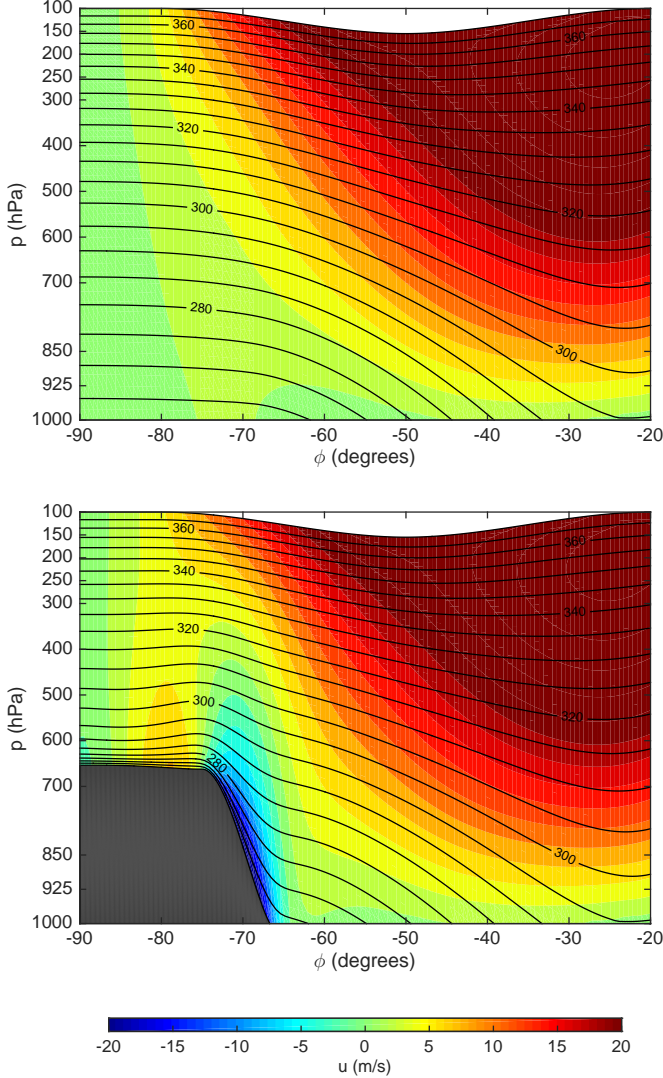


FIG. 8. Solution as in Fig. 7 except with variable top pressure. The maximum westerly wind is approximately  $31 \text{ m s}^{-1}$ ; in the LLJ (bottom panel) the maximum easterly wind is  $26.7 \text{ m s}^{-1}$ .

derstanding the relation of the Antarctic easterly jet with the topography, the potential temperature along the earth's surface, and the interior PV. However, because the divergent flow components do not appear in the PV invertibility principle, this elliptic invertibility problem does not provide insight into the dynamical connections between radiative cooling, katabatic winds, and the topographically bound easterly jet. In this section

we explore these dynamical connections in a qualitative way, leaving a more thorough quantitative analysis for later work.

Within the context of balanced zonal flow, we can understand these connections through the meridional circulation equation and the potential vorticity equation. We begin by noting that, for the zonally symmetric case, the isentropic coordinate version of the mass continuity equation can be written in the form

$$\frac{\partial(\sigma v \cos \phi)}{a \cos \phi \partial \phi} + \frac{\partial(\sigma \dot{\theta} - \partial p / \partial t)}{\partial \theta} = 0, \quad (22)$$

which motivates the representation

$$\sigma v = -\frac{\partial \Psi}{\partial \theta}, \quad \sigma \dot{\theta} - \frac{\partial p}{\partial t} = \frac{\partial(\Psi \cos \phi)}{a \cos \phi \partial \phi}, \quad (23)$$

where  $\Psi$  is the streamfunction for the meridional circulation. The zonal momentum equation can then be written in the form

$$\frac{\partial u}{\partial t} + \dot{\theta} \frac{\partial u}{\partial \theta} + \frac{P}{g} \frac{\partial \Psi}{\partial \theta} = F, \quad (24)$$

where  $F$  denotes the frictional force per unit mass.

Taking  $\partial/\partial t$  and  $\partial/\partial \theta$  of the geostrophic relation  $-fu = \partial M / a \partial \phi$ , and then making use of the hydrostatic relation  $\Pi = \partial M / \partial \theta$ , we obtain

$$\frac{\partial}{a \partial \phi} \left( \frac{1}{\rho \theta} \frac{\partial p}{\partial t} \right) + \frac{\partial}{\partial \theta} \left( f \frac{\partial u}{\partial t} \right) = 0, \quad (25)$$

which is a constraint on the tendencies of the mass and wind fields such that there be a continuous state of hydrostatic and geostrophic balance. Using the second entry in (23) to eliminate  $\partial p / \partial t$ , and then using (24) to eliminate  $\partial u / \partial t$ , we obtain the second order partial differential equation

$$\begin{aligned} \frac{\partial}{a \partial \phi} \left( \frac{1}{\rho \theta} \frac{\partial(\Psi \cos \phi)}{a \cos \phi \partial \phi} \right) + \frac{\partial}{\partial \theta} \left( \frac{f P}{g} \frac{\partial \Psi}{\partial \theta} \right) \\ = \frac{\partial(\Pi, \dot{\theta})}{a \partial(\phi, \theta)} + f \frac{\partial F}{\partial \theta}, \end{aligned} \quad (26)$$

which is elliptic if  $fP > 0$ . Equation (26) describes meridional circulations that are thermally

and frictionally controlled by  $\dot{\theta}$  and  $F$ , and that are shaped by boundary conditions and by the variable coefficients  $(\rho\theta)^{-1}$  and  $fPg^{-1}$ . Although frictional effects do play a role in the dynamics of katabatic winds and the low level easterly jet, the primary forcing for these flow features originates from the  $\dot{\theta}$  term on the right hand side of (26). A simple interpretation of this term can be obtained by noting that it can be expressed in a more concise mathematical form via the relation

$$\frac{\partial(\Pi, \dot{\theta})}{a\partial(\phi, \theta)} = \frac{\partial(\Pi, \dot{\theta})}{a\partial(\phi, p)} \frac{\partial(\phi, p)}{\partial(\phi, \theta)} = \frac{\sigma}{\rho\theta} \left( \frac{\partial\dot{\theta}}{a\partial\phi} \right)_p, \quad (27)$$

where the first equality follows from the Jacobian chain rule, and the second equality from the definition of  $\sigma$ , with the subscript “ $p$ ” indicating that the  $\phi$ -derivative of  $\dot{\theta}$  is taken on an isobaric surface. In other words, the thermal control on the meridional circulation is through the variation of  $\dot{\theta}$  on isobaric surfaces. Thus, a balanced model interpretation of katabatic winds can be obtained by solving (26), with appropriate boundary conditions, for cases in which the  $\dot{\theta}$ -field is dominated by very strong radiative cooling close to the surface ( $\sim 600$  hPa) of the Antarctic plateau. On the 600 hPa isobaric surface the radiative cooling equatorward of  $68^\circ\text{S}$  is much smaller, so that the magnitude of  $(\partial\dot{\theta}/a\partial\phi)_p$  is very large at the edge of the plateau, which would result in a  $\Psi$ -field that is centered near the edge of the plateau, with isolines of  $\Psi$  packed along the sloping topography. Although the elliptic equation (26) has been formulated in  $(\phi, \theta)$ -space, the solution  $\Psi(\phi, \theta)$  can also be used to compute the vertical  $p$ -velocity  $\omega$ , as can be confirmed by noting that

$$\begin{aligned} \omega &= \frac{\partial p}{\partial t} + v \frac{\partial p}{a\partial\phi} + \dot{\theta} \frac{\partial p}{\partial\theta} \\ &= -\frac{1}{\sigma} \frac{\partial\Psi}{\partial\theta} \left( \frac{\partial p}{a\partial\phi} \right)_\theta - \left( \frac{\partial(\Psi \cos\phi)}{a \cos\phi \partial\phi} \right)_\theta \\ &= -\left( \frac{\partial(\Psi \cos\phi)}{a \cos\phi \partial\phi} \right)_p, \end{aligned} \quad (28)$$

where the first equality follows from the definition of  $\omega$ , the second equality follows from (23), and

the final equality from coordinate transformation rules, with the subscript “ $p$ ” again indicating that the  $\phi$ -derivative is taken on an isobaric surface. When isolines of  $\Psi$  are packed along the sloping topography, there is a corresponding katabatic flow with strong subsidence ( $\omega > 0$ ) along the slope.

To see how such slope flows appear in the YOTC analysis, we have constructed cross sections of the  $\omega$ -field, averaged between  $80^\circ$  and  $100^\circ$  E, for both the cold (JJA) and warm (DJF) seasons. These cross-sections, displayed in Fig. 9, reveal large-scale cells with generally weak subsiding motion ( $\omega > 0$ ) in the troposphere and lower stratosphere over the plateau and generally weak rising motion ( $\omega < 0$ ) in the troposphere equatorward of the plateau. Embedded in this large-scale pattern is intense subsidence along the slope, with peak values of  $25.5 \text{ hPa h}^{-1}$  in JJA and  $17.4 \text{ hPa h}^{-1}$  in DJF. The resistance to this intense subsidence is weak because, as can be seen in Fig. 9, it occurs along surfaces of constant potential temperature. As a measure of the intensity of this seasonal mean katabatic flow, we note that the average time required for parcels to descend along the slope from 600 hPa to 1000 hPa is approximately 36 hours for the cold season (JJA) and 48 hours for the warm season (DJF). It is also worth noting that the stronger subsidence values in JJA are consistent with the stronger easterly jet during this period.

It is also interesting to consider the role of radiative cooling in producing the negative PV structures just above the Antarctic plateau in the bottom panels of Fig. 3. The PV equation, derived from the mass continuity equation (22) and the zonal momentum equation (24), can be written in the form

$$\frac{DP}{Dt} = -\frac{g}{\sigma a \cos\phi} \frac{\partial(m, \dot{\theta})}{\partial(\phi, \theta)} - \frac{g}{\sigma} \frac{\partial(F \cos\phi)}{a \cos\phi \partial\phi}, \quad (29)$$

where  $D/Dt$  is the total derivative and  $m = (u + \Omega a \cos\phi) \cos\phi$  is the absolute angular momentum per unit mass. The first term on the right hand side of (29) can be expressed in a somewhat

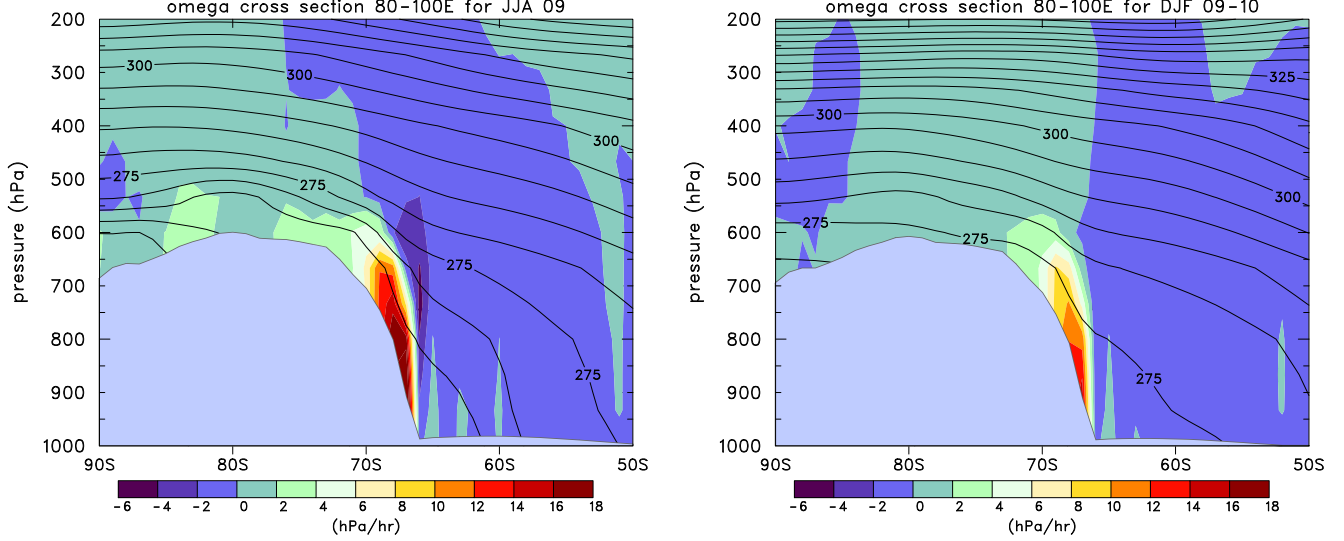


FIG. 9. Mean latitude-pressure cross sections of vertical  $p$ -velocity  $\omega$  (shading, interval  $2 \text{ hPa hr}^{-1}$ ) and potential temperature  $\theta$  (contours, interval  $5 \text{ K}$ ) averaged over the longitude sector  $80\text{--}100^\circ \text{ E}$  from the YOTC analysis for the cold season (JJA, left panel) and warm season (DJF, right panel) as in Fig. 3. For clarity, only the region up to  $200 \text{ hPa}$  and from  $90^\circ \text{ S}$  to  $50^\circ \text{ S}$  is shown.

simpler form via the relation

$$\begin{aligned}
 -\frac{g}{\sigma a \cos \phi} \frac{\partial(m, \dot{\theta})}{\partial(\phi, \theta)} &= -\frac{g}{\sigma a \cos \phi} \frac{\partial(m, \dot{\theta})}{\partial(m, \theta)} \frac{\partial(m, \theta)}{\partial(\phi, \theta)} \\
 &= P \left( \frac{\partial \dot{\theta}}{\partial \theta} \right)_m,
 \end{aligned} \tag{30}$$

where the first equality follows from the Jacobian chain rule, and the second equality from the definition of  $P$ , with the subscript “ $m$ ” indicating that the  $\theta$ -derivative of  $\dot{\theta}$  is taken on an absolute angular momentum surface. Then, just above the strongly negative  $\dot{\theta}$  at the surface of the plateau, we have  $(\partial \dot{\theta} / \partial \theta)_m > 0$ , and since  $P < 0$ , the first term on the right hand side of (29) satisfies  $P(\partial \dot{\theta} / \partial \theta)_m < 0$ , which is consistent with the large negative PV (less than  $-20 \text{ PVU}$  for JJA) shown in the bottom two panels of Fig. 3. As we have shown, this negative PV over the plateau is an important part of the specified data for the PV invertibility problem (10)–(14). For the zonally symmetric case, this specified data also includes

the topography  $\Phi_S(\phi)$  and the potential temperature along the topography,  $\theta_S(\phi)$ . If the interior PV anomaly is not included in the specified data for the invertibility problem, the specified  $\Phi_S(\phi)$  and  $\theta_S(\phi)$  produce an the easterly jet that is too strong. Thus, the role of radiative cooling is to produce a  $\theta_S(\phi)$  field that is nearly constant along the continental slope and also a PV anomaly just above the plateau, both of which contribute to the structure and strength of the easterly jet.

## 7. Concluding remarks

We have argued that the topographically bound low-level jet surrounding Antarctica is produced by the unique large-scale, ice-dome topography of the continent and is dynamically connected to the radiatively driven katabatic flows. We have shown that this low-level easterly jet can be modeled as a balanced flow, with the balanced wind and thermal structure in and around the jet being determined by the topography, the distribution of potential temperature along the topography, and the potential vorticity in the fluid interior. We

have also argued that the meridional circulation can be modeled in terms of an Eliassen-type elliptic equation with the frictional and katabatic effects concentrated near the lower boundary. It is interesting to note that the dynamical arguments used here for the Antarctic circulation are very similar to those used by Schubert et al. (1991) in modeling the PV dynamics of the ITCZ and the tropical Hadley circulation. While the fundamental balanced dynamics of these two meridional circulation cells are similar, the diabatic forcing processes are quite different, with the tropical Hadley cell forced primarily by deep moist convection and the Antarctic cell forced primarily by shallow radiative processes.

The conceptual framework introduced in section 6 treats the entire meridional flow as forced primarily by low-level katabatic and frictional processes. This elliptic formulation of the problem provides a filtered view of the meridional circulation since transient inertia-gravity waves are not allowed. It is interesting to note that this mathematical formulation of the meridional circulation problem, while capturing the essence of the large scale dynamics, misses an interesting aspect of the observed Antarctic flow. This aspect is often referred to as a “katabatic jump” or “Loewe’s phenomenon”, which occurs near the Antarctic coastline when strong katabatic flow off the elevated terrain experiences a sudden slowing down and a sudden increase in the depth of the katabatic layer, as documented in the two examples discussed by Pettré and André (1991). The pioneering work of Ball (1956, 1957) provides an explanation in terms of hydraulic jump theory, with the upstream “shooting flow” having a Froude number greater than unity and the downstream “tranquil flow” having a Froude number less than unity. More recently this flow phenomenon has been modeled by Gallée and Schayes (1992, 1994) and Gallée et al. (1996) using a hydrostatic numerical model and by Yu et al. (2005) using a non-hydrostatic numerical model.

The reason the meridional circulation theory of section 6 misses the katabatic jump phenomenon

is that the theory uses a local dynamical balance, i.e., the meridional advection term is neglected in the meridional momentum equation. Inclusion of this horizontal advection term changes the mathematical nature of the problem in the sense that the equations become hyperbolic, so the solution can be obtained via the method characteristics, with the possibility of intersection of characteristics and the formation of discontinuities in the wind field. In this regard there is a certain analogy with the dynamics of tropical cyclones. Ooyama (1969) showed that the essence of tropical cyclone dynamics can be described by an axisymmetric, gradient-balanced model, with a nearly inviscid interior and a local Ekman-type boundary layer theory providing the lower boundary condition for the transverse circulation in the interior. This model misses the phenomenon of tropical cyclone boundary layer shocks. However, when the local Ekman-type boundary layer model is generalized to include the horizontal advection terms, the boundary layer equations take a hyperbolic form, allowing the formation of near discontinuities in the boundary layer radial inflow and near singularities in the boundary layer pumping. The implications of this for the formation of primary and secondary eyewalls is discussed by Williams et al. (2013) and Slocum et al. (2014). While the formation of boundary layer shocks can play a crucial role in the eyewall dynamics of tropical cyclones, the formation of katabatic jumps near the Antarctic continental edge probably plays a less-crucial role in the overall dynamics of the Antarctic circulation.

#### *Acknowledgments.*

We would like to thank Levi Silvers, Chris Slocum, and Rick Taft for their valuable advice and for assistance with the figures. The reanalysis data used in creating Figs. 2 and 3 was provided by the European Centre for Medium-Range Weather Forecasts. This research was supported by the National Science Foundation under a collaborative grant with award number AGS-1147431

to Clarkson University and award number AGS-1147120 to Colorado State University.

## APPENDIX

### Numerical solution

The zonally-symmetric version of the problem (10)–(14) is solved numerically using a multigrid method based on a finite difference discretization as follows. To discretize the problem we introduce the grid points  $(\phi_j, \theta_k) = (\phi_S + j\Delta\phi, \theta_B + k\Delta\theta)$  with  $j = 0, 1, \dots, m$  and  $k = 0, 1, \dots, n$ , where  $\Delta\phi = (\phi_N - \phi_S)/m$  and  $\Delta\theta = (\theta_T - \theta_B)/n$ . We then seek an approximate solution with grid-point values  $\psi_{j,k} \approx \psi(\phi_j, \theta_k)$  satisfying the discrete equation

$$\alpha_{j,k} \left( \frac{a_j \psi_{j-1,k} - d_j \psi_{j,k} + b_j \psi_{j+1,k}}{a^2 \Delta\phi^2} \right) + f_j \left( \frac{\psi_{j,k-1} - 2\psi_{j,k} + \psi_{j,k+1}}{\Delta\theta^2} \right) = F_{j,k}, \quad (\text{A1})$$

where  $f_j = 2\Omega \sin \phi_j$ ,

$$\alpha_{j,k} = \begin{cases} \frac{g}{\theta_k \rho_{j,k} P_{j,k}}, & \theta_S(\phi_j) < \theta_k < \theta_T, \\ 0, & \theta_B < \theta_k < \theta_S(\phi_j), \end{cases} \quad (\text{A2})$$

and

$$F_{j,k} = \frac{\tilde{\sigma}_k}{\theta_k \tilde{\rho}_k} - \alpha_{j,k} f_j, \quad (\text{A3})$$

with  $P_{j,k} = P(\phi_j, \theta_k)$ ,  $\tilde{\sigma}_k = \tilde{\sigma}(\theta_k)$ , and  $\tilde{\rho}_k = \tilde{\rho}(\theta_k)$ . The values  $\rho_{j,k}$  are related to the solution values  $\psi_{j,k}$  via

$$\rho_{j,k} = \frac{p_0}{R\theta_k} \left( \frac{\Pi_{j,k}}{c_p} \right)^{c_v/R} \quad (\text{A4})$$

and

$$\Pi_{j,k} = \tilde{\Pi}_k + f_j \left( \frac{\psi_{j,k+1} - \psi_{j,k-1}}{2\Delta\theta} \right) \quad (\text{A5})$$

with  $\tilde{\Pi}_k = \tilde{\Pi}(\theta_k)$ . At the interior points  $j = 1, \dots, m-1$  the discretization of the Laplacian appearing in (A1) is based on (15), giving

$$a_j = \frac{c_{j-1/2}}{c_j}, \quad b_j = \frac{c_{j+1/2}}{c_j}, \quad d_j = a_j + b_j, \quad (\text{A6})$$

where  $c_j = \cos \phi_j$  and  $c_{j\pm 1/2} = \cos \phi_{j\pm 1/2}$ . At the south pole  $j = 0$  the discretization is based on (16), giving  $a_j = b_j = 2$  and  $d_j = 4$ , where we have introduced the ghost point  $j = -1$  with the corresponding value determined by the symmetry condition  $\psi_{-1,k} = \psi_{1,k}$ . At the north boundary  $j = m$  we specify  $\psi_{j,k}$  as described in section 2. For the top and bottom boundary conditions we introduce the ghost points  $k = -1$  and  $k = n+1$  and approximate the vertical boundary conditions (A7) and (A8) using centered differences as

$$f_j \left( \frac{\psi_{j,n+1} - \psi_{j,n-1}}{2\Delta\theta} \right) = \Pi_T(\phi_j) - \tilde{\Pi}_T(\phi_j), \quad (\text{A7})$$

and

$$f_j \left[ \psi_{j,0} - \theta_B \left( \frac{\psi_{j,1} - \psi_{j,-1}}{2\Delta\theta} \right) \right] = \Phi_S(\phi_j) \quad (\text{A8})$$

for  $j = 0, \dots, m-1$ , where  $\Pi_T(\phi_j)$  and  $\Phi_S(\phi_j)$  are the specified boundary values. Thus, the interior equation (A1) is applied for  $j = 0, \dots, m-1$  and  $k = 0, \dots, n$ .

The discrete system (A1)–(A8) is quasilinear, due to the dependence of  $\rho$ —and hence  $\alpha$ —on  $\psi$ . Since the system is large and sparse, it is best solved by an iterative method. We use a multigrid method, similar to that of Chen and Fulton (2010). On each grid the discrete equation (A1) is relaxed using alternating direction line relaxation, holding the ghost-point values fixed during each sweep and then updating them after the sweep via the boundary conditions. This relaxation is embedded in a  $V$ -cycle control algorithm, with residuals transferred to coarser grids using full weighting and corrections transferred to finer grids using bilinear interpolation. The density  $\rho$  is held fixed during each cycle and then updated on the finest grid after the cycle via (A4) and (A5). This method achieves typical multigrid efficiency, i.e., residuals are reduced by a factor of about 0.6 per sweep independent of the mesh size. Typically only three  $V$ -cycles are needed to achieve sufficient accuracy.

The results presented here we computed using a finest grid with  $m \times n = 1024 \times 512$  grid intervals,

giving mesh size  $0.068^\circ$  in latitude (approximately 7.6 km) and 0.21 K in  $\theta$ . Eight coarser grids are used. Once the streamfunction is computed, the wind field can be computed from

$$u_{j,k} = - \left( \frac{\psi_{j+1,k} - \psi_{j-1,k}}{2a\Delta\phi} \right) \quad (\text{A9})$$

and the pressure field can be computed from (A5) and the definition of  $\Pi$ .

## REFERENCES

- Ball, F. K., 1956: The theory of strong katabatic winds. *Austral. J. Phys.*, **9**, 373–386.
- Ball, F. K., 1957: The katabatic winds of Adélie Land and King George Island. *Tellus*, **9**, 201–208.
- Ball, F. K., 1960: Winds on the ice slopes of Antarctica. *Proceedings of the Symposium on Antarctic Meteorology*, Melbourne, Australia, Pergamon Press, New York, 9–16.
- Charney, J. G. and M. E. Stern, 1962: On the stability of internal baroclinic jets in a rotating atmosphere. *J. Atmos. Sci.*, **19**, 159–172.
- Chen, Y. and S. R. Fulton, 2010: An adaptive continuation-multigrid method for the balanced vortex model. *J. Comput. Phys.*, **229**, 2236–2248.
- Egger, J., 1985: Slope winds and the axisymmetric circulation over Antarctica. *J. Atmos. Sci.*, **42**, 1859–1867.
- Eliassen, A., 1980: Balanced motion of a stratified, rotating fluid induced by bottom topography. *Tellus*, **32**, 537–547.
- Fulton, S. R. and W. H. Schubert, 1991: Surface frontogenesis in isentropic coordinates. *J. Atmos. Sci.*, **48**, 2534–2541.
- Gallée, H., P. Pettré, and G. Schayes, 1996: Sudden cessation of katabatic winds in Adélie Land, Antarctica. *J. Appl. Meteor.*, **35**, 1142–1152.
- Gallée, H. and G. Schayes, 1992: Dynamical aspects of katabatic wind evolution in the Antarctic coastal zone. *Boundary-Layer Meteorology*, **59**, 141–161.
- Gallée, H. and G. Schayes, 1994: Development of a three-dimensional meso- $\gamma$  primitive equation model: Katabatic winds simulation in the area of Terra Nova Bay, Antarctica. *Mon. Wea. Rev.*, **122**, 671–685.
- Hoskins, B. J. and K. I. Hodges, 2005: A new perspective on Southern Hemisphere storm tracks. *J. Climate*, **18**, 4108–4129.
- Inatsu, M. and B. J. Hoskins, 2004: The zonal asymmetry of the Southern Hemisphere winter storm track. *J. Climate*, **17**, 4882–4891.
- King, J. C. and J. Turner, 1997: *Antarctic Meteorology and Climatology*. 1st ed., Cambridge Atmospheric and Space Science Series, Cambridge University Press, 409 pp.
- Kottmeier, C. and H.-U. Stuckenberg, 1986: Quasi-geostrophic flow solution for the circulation over Antarctica. *Beitr. Phys. Atmosph.*, **59**, 491–504.
- Kuo, H. L., 1959: Finite amplitude three-dimensional harmonic waves on the spherical earth. *J. Meteor.*, **16**, 524–534.
- Mather, K. B., 1969: The pattern of surface wind flow in Antarctica. *Pure Appl. Geophys.*, **75**, 332–354.
- Mather, K. B. and G. S. Miller, 1967: Notes on topographic factors affecting the surface wind in Antarctica, with special reference to katabatic winds, and bibliography (Antarctic topographic effects on prevailing surface winds). University of Alaska Tech. Rep. No. GA-900, 63 pp., Fairbanks, Alaska.

- Ooyama, K., 1969: Numerical simulation of the life cycle of tropical cyclones. *J. Atmos. Sci.*, **26**, 3–40.
- Parish, T. R. and D. H. Bromwich, 1987: The surface wind field over the Antarctic ice sheets. *Nature*, **328**, 51–54.
- Pettré, P. and J.-C. André, 1991: Surface-pressure change through Loewe’s phenomena and katabatic flow jumps: Study of two cases in Adélie Land, Antarctica. *J. Atmos. Sci.*, **48**, 557–571.
- Schubert, W. H., P. E. Ciesielski, D. E. Stevens, and H.-C. Kuo, 1991: Potential vorticity modeling of the ITCZ and the Hadley circulation. *J. Atmos. Sci.*, **48**, 1493–1509.
- Schubert, W. H. and M. T. Masarik, 2006: Potential vorticity aspects of the MJO. *Dyn. Atmos. Oceans*, **42**, 127–151.
- Schubert, W. H., R. K. Taft, and L. G. Silvers, 2009: Shallow water quasi-geostrophic theory on the sphere. *J. Adv. Model. Earth Syst.*, **1**, Art. #2.
- Silvers, L. G. and W. H. Schubert, 2013: A theory of topographically bound balanced motions and application to atmospheric low-level jets. *J. Atmos. Sci.*, **69**, 2878–2891.
- Slocum, C. J., G. J. Williams, R. K. Taft, and W. H. Schubert, 2014: Tropical cyclone boundary layer shocks. *arXiv:1405.0304 [physics.aoph]*, **1405**, May 13.
- Smith, R. B., 1979: The influence of mountains on the atmosphere. *Adv. Geophys.*, **21**, 87–230.
- Waliser, D. E., M. Moncrieff, D. Burridge, and Coauthors, 2012: The ‘Year’ of tropical convection (May 2008 to April 2010): Climate variability and weather highlights. *Bull. Amer. Meteor. Soc.*, **93**, 1189–1218.
- Williams, G. J., R. K. Taft, B. D. McNoldy, and W. H. Schubert, 2013: Shock-like structures in the tropical cyclone boundary layer. *J. Adv. Model. Earth Syst.*, **5**, 338–353.
- Yu, Y., X. Cai, J. C. King, and I. A. Renfrew, 2005: Numerical simulations of katabatic jumps in Coats Land, Antarctica. *Boundary-Layer Meteorology*, **114**, 413–437.
- Zwally, H. J., J. C. Comiso, C. L. Parkinson, W. J. Campbell, F. D. Carsey, and D. Cloersen, 1983: Antarctic Sea Ice, 1973–1976, Satellite passive microwave observations. National Aeronautics and Space Administration, Washington D. C.